Journal of
Materials Chemistry A

Materials for energy and sustainability

Accepted Manuscript

This article can be cited before page numbers have been issued, to do this please use: J. M. Palomo and C. Garcia-Sanz, *J. Mater. Chem. A*, 2026, DOI: 10.1039/D6TA03387C.

ROYAL SOCIETY OF CHEMISTRY

rsc.li/materials-a

View Article Online
DOI: 10.1039/D6TA03387C

Synthesis and design of Nickel-Enzyme Ligand Framework for adsorption and catalytic degradation of environmental pollutants

Carla Garcia-Sanz[1] and Jose M. Palomo*,[1]

[1] Instituto de Catalisis y Petroleoquimica (ICP), CSIC, c/Marie Curie 2, 28049 Madrid (Spain)

*Correspondence: josempalomo@icp.csic.es

View Article Online
DOI: 10.1039/D6TA03387C

Abstract

Metal–organic frameworks (MOFs) are versatile porous materials with tunable structures and functionalities. Here, we report the *in situ* construction of MOF elements through the direct participation of enzymes as ligands during framework formation (ELF), using aqueous media and at room temperature. While conventional Ni-MOFs displayed compact morphologies, enzyme-assisted synthesis generated well-defined snowflake-like microstructures, with enzyme size governing the final architecture. Larger enzymes promoted the formation of sandwich-like layered structures.

Structural characterization confirmed porous materials with pore diameters of 3–6 nm, pore volumes of 0.17–0.22 cm^3/g, and surface areas ranging from 82 to 139 m^2/g. Fluorescent labeling revealed preferential enzyme localization at the periphery of the flakes while preserving accessibility to the central region, yielding a hierarchical hybrid porous material with enhanced functional organization.

The materials were evaluated for adsorption of aquatic micropollutants, including rhodamine B, phenol, p-aminophenol, and p-benzoquinone. Ni-ELF 1 showed the highest adsorption capacity, reaching 300 ppm/h. As a proof of concept, Ni-ELF 1 also catalyzed the hydrolytic degradation of PET bottle fragments, producing 135 nmol of degradation products·mL^{-1}·day^{-1}.

Keywords: MOFs, hybrid, enzyme, porous material, nickel, adsorption, micropollutants.

View Article Online
DOI: 10.1039/D6TA03387C

Introduction

Metal–organic frameworks (MOFs) constitute a versatile family of porous materials defined by three-dimensional networks in which metal ions or clusters act as nodes connected through coordination bonds to polydentate organic ligands.[1-4] This hybrid architecture endows MOFs with distinctive properties that set them apart from other porous materials such as zeolites or mesoporous silicas: exceptionally high micro-/mesoporous volume, tunable structural diversity, relatively straightforward synthesis, adjustable surface functionalization, and, in many cases, notable biocompatibility.[5-8] The wide array of available linkers — including carboxylates, nitrogen-containing ligands, phosphonates, sulfonates, and cyano groups — enables the construction of architectures with varied morphologies (1D, 2D, or 3D), spanning from flexible nanosheets to highly ordered and complex crystalline networks.[9-12]

In recent years, an innovative trend has emerged at the interface of coordination chemistry and biology: Biological Metal–Organic Frameworks (BioMOFs).[13-14] These materials represent an advanced generation of MOFs that incorporate biomolecules — such as amino acids, peptides, nucleotides or sugars—into their framework. [15-18] By replacing or complementing conventional synthetic linkers, biological components introduce functionalities that are otherwise difficult to achieve, including chirality, specific recognition motifs, redox-active groups, and catalytic sites inspired by natural systems. Consequently, BioMOFs offer unique opportunities in biocatalysis, biosensing, drug delivery, and environmental remediation.[19-21]

One of the main advantages of BioMOFs lies in the intrinsic integration of biological compatibility and functionality into the framework structure. By merging the structural precision of MOFs with the complexity of biomolecules, these hybrid materials achieve

View Article Online
DOI: 10.1039/D6TA03387C

enhanced stability in aqueous environments, increased selectivity toward target substrates, and cooperative effects between inorganic nodes and biological linkers.[22-23] However, it is important to note that most BioMOF-based systems reported to date focus mainly on two approaches: the encapsulation of biomolecules within pre-formed frameworks and the immobilization of enzymes onto MOF surfaces. In both cases, the biomolecule acts as a guest or attached species, benefiting from the protective microenvironment or enhanced stability provided by the porous scaffold, but without influencing the structural organization of the material.[24-26]

In contrast, a far less explored and conceptually transformative strategy involves the direct participation of the biomolecule—particularly enzymes—as an integral structural component of the framework itself. In such systems, the enzyme is not merely confined or immobilized but actively participates in the coordination process during MOF formation, serving as a true biological building block. This integration opens unprecedented possibilities for tailoring the physicochemical properties, catalytic behavior, and structural dynamics of the resulting BioMOFs, moving beyond passive encapsulation toward active structural and functional synergy between the biological and inorganic domains.

In line with this concept, our research group has developed a strategy to engineer nanobiohybrid systems through the *in-situ* formation of metal nanoparticles, templated and controlled by the intrinsic structure of proteins.[27,28] Here, this approach is conceptually extended by integrating the three-dimensional architecture of the protein into the formation of an ordered two-dimensional reticular framework.

View Article Online
DOI: 10.1039/D6TA03387C

We define this new class of materials as Enzyme–Ligand Frameworks (ELFs), in which the enzyme acts as an integral structural node within the framework. This design moves beyond conventional BioMOFs—where biomolecules are typically encapsulated or superficially immobilized—by embedding the biological component directly into the framework architecture, thereby enabling a synergistic interplay between structure and function.

Nickel was selected as the metal node because Ni-based MOFs combine high structural stability with versatile coordination chemistry, enabling their use in a wide range of applications, including CO_2 valorization, energy storage, and heterogeneous catalysis.[30,31]

MOF-based composites have emerged as highly efficient platforms for environmental remediation, particularly in wastewater treatment, owing to their high surface area, tunable porosity, and ability to interact with a wide range of pollutants.[32,33] Wastewater streams contain complex mixtures of contaminants, including pharmaceuticals and synthetic dyes, which are persistent and resistant to conventional treatment methods.[34,35] Among the available technologies, adsorption stands out as one of the most effective and sustainable approaches due to its operational simplicity, low energy requirements, and broad applicability.[36,37] In this context, MOF composites offer significant advantages over pristine MOFs, as the incorporation of complementary components can enhance structural stability, surface reactivity, and the availability of tailored active sites, thereby enabling multiple adsorption mechanisms.[38-40]

Within this framework, the development of Ni–ELF materials provides a promising strategy to design advanced adsorbents in which the enzyme-derived functionality and the metal-organic network act cooperatively to enhance pollutant capture.[41] Such systems

View Article Online
DOI: 10.1039/D6TA03387C

are particularly attractive for the removal of emerging contaminants, including pharmaceuticals and dyes, and may also be extended to other persistent pollutants such as polyethylene terephthalate (PET), a widely used plastic whose accumulation remains a major environmental concern due to its low recycling rates.[42-43]

Herein, we investigate Ni–ELF materials as a novel class of biohybrid adsorbents for the efficient removal of diverse contaminants from aqueous media, highlighting the potential of this approach for next-generation water purification technologies and assessing their ability to degrade plastic waste.

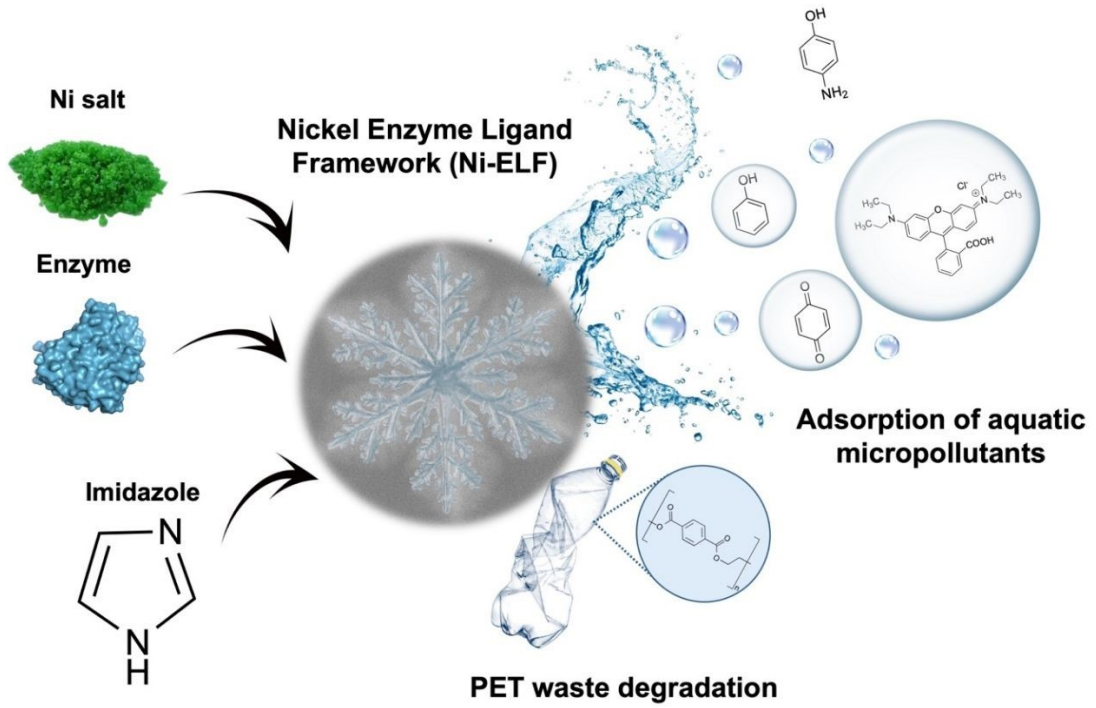

Figure 1. Schematic overview of the proposed Ni–ELF system and its targeted applications.

View Article Online
DOI: 10.1039/D6TA03387C

Experimental section

Chemicals

Nickel (II) chloride hexahydrate ($NiCl_2 \cdot 6H_2O$), imidazole, Rhodamine B (RhB), *p*-aminophenol (*p*AP), *p*-benzoquinone (*p*-BQ), phenol, Alexa fluor 700 and Triton® X-100 were purchased from Sigma-Aldrich (MA, USA). Hydrogen peroxide (H_2O_2 30% v/v) was from Labkem (Barcelona, Spain). Hydrochloric acid (37% v/v) was purchased from Panreac AppliChem (Barcelona, Spain). Lipase B from *Candida antarctica* (Lipozyme® CalB, CALB), catalase (Catazyme 25 L, CAT), and glucose oxidase (Gluzyme® Mono 10000 BG, GOx) were obtained from Novonesis (formerly Novozymes, Bagsvaerd, Denmark). PET plastic bottle was obtained from Fuente Dehesa (Extremadura, Spain).

Instrumentation

Spectrophotometric analyses were performed using a V-730 spectrophotometer (JASCO, Tokyo, Japan), while infrared (IR) measurements of Ni-ELF were conducted using an FT/IR-4600 spectrophotometer (JASCO, Tokyo, Japan). The Ni content in the solid material was determined through Inductively Coupled Plasma-Optical Emission Spectroscopy (ICP-OES). For this analysis, 5 mg of the solid powder was digested in 6 mL of HCl (37% v/v), followed by the addition of 44 mL of water. The mixture was centrifuged, and the clear supernatant was analyzed using an Avio 220 Max ICP-OES instrument in axial mode (λ = 231.604) (PerkinElmer, Waltham, MA, USA). X-ray diffraction (XRD) patterns were obtained using a PANalytical X'Pert Pro polycrystalline X-ray diffractometer, equipped with a D8 Advance analysis texture configuration (Bruker, Billerica, MA, USA) and Cu Kα radiation (λ = 1.5406 Å, 45 kV, 40 mA). Data

View Article Online
DOI: 10.1039/D6TA03387C

processing was performed with X'Pert Data Viewer and X'Pert Highscore Plus software. The size and morphology of Ni-ELF was analyzed using scanning electron microscopy (SEM) with a TM-1000 microscope (Hitachi, Tokyo, Japan).

For sample preparation, a small amount of the material was deposited onto a thin film with a conductive carbon coating. Surface area and pore size distribution were determined by isothermal nitrogen (N_2) adsorption/desorption using BHJ desorption and analyzed with Microactive 5.02 software. Thermal stability and plastic degradation reactions were studied using an Opa Q incubator equipped with an OL30 ME orbital shaker.

Confocal images were acquired using a Leica Stellaris 8 microscope (Wetzlar, Germany) equipped with two FLIM (Fluorescence Lifetime Imaging Microscopy) modules and two depletion lasers (592 nm and 775 nm).

General synthesis of Ni-ELF BioMOFs

0.53 mL of commercial CALB solution (10 mg/mL, determined by the Bradford assay), 0.35 mL of catalase solution (31 mg/mL, determined by the Bradford assay), or 110 mg of GOx powder (equivalent to 10.8 mg enzyme per 100 mg powder) was added to 20 mL of 0.1 M sodium bicarbonate buffer at pH 10, yielding a final enzyme concentration of 0.3 mg/mL. The preparation was carried out in a 60 mL glass bottle containing a small magnetic stir bar. Subsequently, 800 mg of imidazole was added to the mixture. Upon the addition of 200 mg of $NiCl_2 \cdot 6H_2O$, a noticeable color change was observed, producing a cloudy, light purple solution. The pH of the mixture decreased to 9. The solution was stirred at room temperature for 30 minutes. Afterward, the mixture was centrifuged at 8000 rpm for 5 minutes, and the recovered pellet was washed three times with distilled water (3 x 10 mL). Finally, the supernatant was discarded, and the pellet from each Falcon tube was resuspended in 2 mL of water, collected in a cryotube, frozen in liquid nitrogen,

View Article Online
DOI: 10.1039/D6TA03387C

and lyophilized for 28 h. The resulting Ni-ELFs (Enzyme–Ligand Frameworks) were obtained as pale green solids (Figure S1). The final lyophilized materials were designated as **Ni-ELF 1** (CALB-based, 0.372 g), **Ni-ELF 2** (GOX-based, 0.396 g), and **Ni-ELF 3** (catalase-based, 0.368 g).

Labeling of CALB with Alexa Fluor

The labeling of CALB with Alexa Fluor 700 (AF) was performed using 1.5 equiv. of AF relative to the amount of enzyme. To prepare the dye solution, AF was dissolved in DMSO to achieve a concentration of 1 mg/mL relative to the enzyme amount**,** and the solution was protected from light with aluminum foil due to the dye's light sensitivity. Subsequently, 772 µL of the AF working solution were added to 5 mL of a CALB solution (2.5 mg/mL) prepared in 0.1 M sodium bicarbonate buffer, pH 8.0. The mixture was incubated for 3 hours at room temperature, protected from light with aluminum foil. The labeling occurs through covalent attachment of AF to the N-terminal amino group of the enzyme. The reaction progress was monitored by UV–Vis spectroscopy: free AF showed an absorption maximum at 715 nm, whereas conjugated AF shifted to 695 nm. Complete labeling was achieved after 1 hour, as no further changes in absorbance were observed over time. The conjugate was purified by dialysis against distilled water in the dark, with foil protection, replacing the water three times at 30-minute intervals. After dialysis, the protein concentration was 1.84 mg/mL, indicating slight dilution. The labeled enzyme was stored at 4 °C, protected from light. The purified AF–CALB conjugate was then used for the preparation of the Ni-ELF 1 BioMOF following the standard synthesis procedure.

View Article Online
DOI: 10.1039/D6TA03387C

Adsorption of Aquatic Micropollutants on the BioMOF

The adsorption capacity of the BioMOF was evaluated using several model aqueous contaminants. In a typical experiment, 10 mg of Ni-ELF were incubated with 2 mL of aqueous contaminant solutions at the following concentrations: 10 ppm Rhodamine B (RhB), 100 ppm benzoquinone, 100 ppm *p*-aminophenol, or 100 ppm phenol.

Suspensions were kept under magnetic stirring at room temperature, and aliquots were withdrawn at predetermined time intervals. Prior to analysis, the aliquots were centrifuged to remove the BioMOF, ensuring that only the dissolved contaminants were measured. The adsorption of the contaminants onto the BioMOF was monitored by UV–Vis spectroscopy using a quartz cuvette over a spectral range of 200–600 nm. The adsorption process was quantified by tracking the decrease in the characteristic absorption peak of each contaminant relative to its initial intensity.

The characteristic absorption maxima used for analysis were 555 nm for Rhodamine B, 246 nm for benzoquinone, 270 nm for phenol, and 297 nm for *p*-aminophenol. The removal efficiency (RE), which represents the fraction of pollutant removed from the solution after the adsorption process, was calculated using the following equation:

$$\%RE = \frac{C_O - C_T}{C_O} \cdot 100$$

where C_o and C_T are the initial and time-dependent contaminant concentrations, respectively.

The adsorption capacity at equilibrium, q*e* (mg pollutant/g BioMOF), was determined using the following equation:

View Article Online
DOI: 10.1039/D6TA03387C

$$q_e = \frac{(C_O - C_e)\cdot V}{m}\cdot 100$$

where C_e is the equilibrium concentration of the contaminant (mg/L), VV is the solution volume (L), and mm is the mass of BioMOF (g).

The adsorption kinetics were analyzed using the pseudo-second order (PSO) model, which assumes that the rate-limiting step is chemisorption. The PSO model is described by the linearized equation:

$$\frac{t}{q_t} = \frac{1}{k_2 q_e^2} + \frac{t}{q_e}$$

Where q_t ($mg\cdot g^{-1}$) is the amount of contaminant adsorbed at time t, q_e is the adsorption capacity at equilibrium, and k_2 ($g\cdot mg^{-1}\cdot min^{-1}$) is the PSO rate constant. By plotting t/qt versus t both q_e and k_2 can be obtained from the slope and intercept of the linear fit.

Degradation of PET

The degradation of polyethylene terephthalate (PET) was investigated using Ni–ELF 1. PET samples (either 4 cm² or 1 cm² pieces sourced from a plastic bottle) were placed in 20 mL glass vials containing 10 mL of distilled water using 20 mg of Ni–ELF 1.

In some experiments, either 0.025% v/v Triton X-100 or 0.1 M NaOH was added. The vials were continuously stirred at room temperature for 28 days to monitor the degradation process. To monitor PET degradation, UV-Vis spectroscopy was performed weekly on the supernatant in the 240–800 nm range using a quartz cuvette to detect changes in the absorption spectrum. Scanning electron microscopy (SEM) was employed

View Article Online
DOI: 10.1039/D6TA03387C

to analyze PET fragmentation into smaller particles (microplastics), while Fourier transform infrared (FT-IR) spectroscopy was used to identify chemical modifications indicative of polymer degradation. The extent of PET degradation was determined by measuring the sample's weight before and after the reaction, and the percentage of degradation was calculated. The weight loss (w/w %) of PET was determined using the following formula:

$$Weightloss\ (\%) = \frac{m_0 - m_f}{m_0} x100$$

where m_0 (mg) and m_f (mg) represent the total mass of the PET sample before and after 28 days of reaction, respectively.

Additionally, the number of degraded moles of PET was calculated using the following formula:

$$Moles\ of\ degrated\ PET = \frac{(m_0 - m_f)}{M_{PET}}$$

where M_{PET} is the molecular weight of PET, taken as 192 g/mol. This formula allows for determining the number of moles of PET degraded based on the weight loss percentage observed in the reaction.

A variation of this assay involved cutting a 1 cm² PET piece into smaller portions, which were incubated in 15 mL of water containing 0.025% v/v Triton X-100 and 300 mg of Ni–ELF 1. This mixture was incubated at 60ºC for 93 h in a silicone bath. Degradation was monitored as described above (UV–Vis, FT–IR, SEM), and the percentage of PET degradation was calculated in the same manner as in the previous experiments.

View Article Online
DOI: 10.1039/D6TA03387C

Results and discussion

Synthesis and Characterization of Ni-ELF BioMOFs

First, the Ni-ELF BioMOFs were designed using enzymes with diverse nature, conformational structures, and sizes, including monomeric, dimeric, and tetrameric complexes. The synthesis was carried out through a simple, environmentally friendly, one-step method using 0.3 mg/mL of the enzyme (lipase from *Candida antarctica* B (CALB, 33 kDa), glucose oxidase (GOx, 160 kDa), or catalase (240 kDa)) in sodium bicarbonate aqueous buffer (pH 10). This solution was incubated with imidazole (40 mg/mL) and nickel chloride hexahydrate ($NiCl_2 \cdot 6H_2O$, 10 mg/mL) for 30 minutes at room temperature (Figure 2).

The metal/enzyme and ligand ratios were selected based on previously reported protocols from our group and literature precedents on enzyme–metal coordination systems, which consistently provide reproducible formation of active ELF materials while maintaining enzyme stability.[17,27-28.]

Upon nickel addition, the solution turned a cloudy lilac color, indicating the coordination of Ni^{2+} with imidazole and the enzyme, consistent with a partially octahedral geometry.[44] This color change suggests the formation of the hydrated complex $[Ni(Imidazole)_4(H_2O)_2]^{2+}$, with nickel coordinated with the protein. Longer incubation times (1, 3 and 17 hours) produced the same structure and metal content, confirming that 30 minutes was optimal. The resulting solid was collected by centrifugation, washed with distilled water, frozen, and lyophilized.

After lyophilization, the solid exhibited a pale green color, typically associated with octahedral complexes.[45] This transition suggests the removal of water molecules and the

View Article Online
DOI: 10.1039/D6TA03387C

formation of the pure octahedral complex $[Ni(Imidazole)_6]^{2+}$. The green coloration likely reflects a more rigid geometry and crystal field effects within the Ni-ELF structure, which also involves the protein. The final lyophilized solids were designated as **Ni-ELF 1** (CALB-based), **Ni-ELF 2** (GOx-based), and **Ni-ELF 3** (catalase-based).

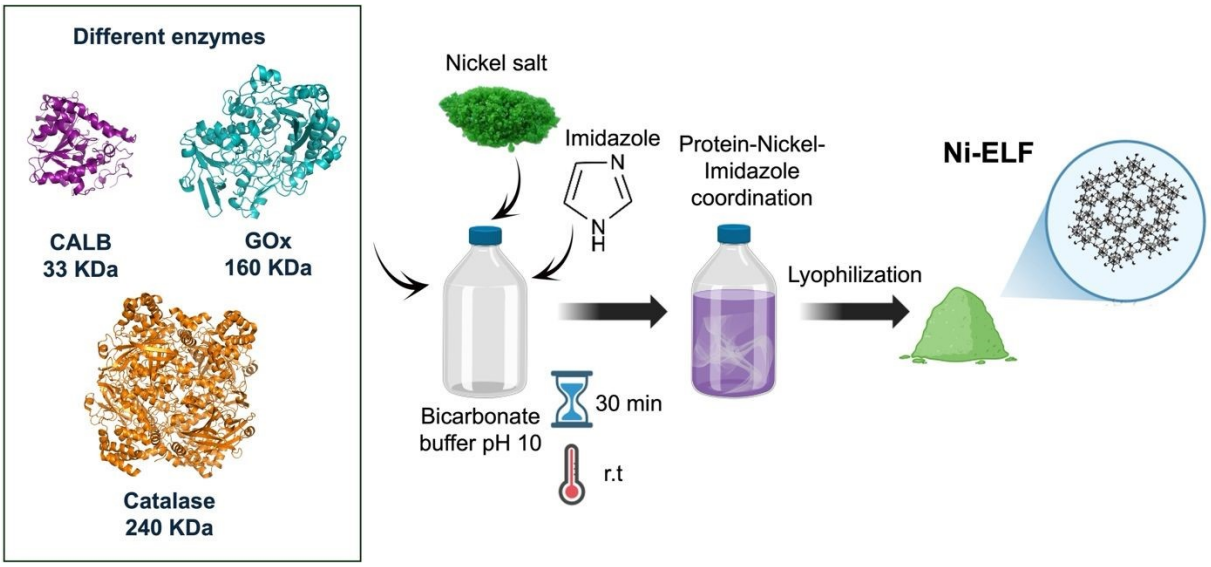

Figure 2. Schematic illustration of the room-temperature aqueous-phase synthesis of Ni-ELF BioMOFs using different enzymes.

Subsequently, SDS-PAGE electrophoresis was performed on the supernatant from the synthesis to assess the amount of enzyme bound to the ELF system**.** The results revealed that 76% of the provided enzyme was incorporated into the designed system during synthesis (Figure S2).

Next, wide-angle X-ray diffraction (XRD) was used to characterize the Ni-ELF BioMOFs (Figure 3a). The analyses revealed similar diffraction patterns for all samples, showing high crystallinity with peaks at 2θ values of 13.8º, 20º, 23.8º, and 31º, corresponding to nickel-imidazole coordination.[46] The presence of these species was further confirmed using Fourier Transform Infrared Spectroscopy (FT-IR) (Figure 3b, Figure S4). The key

View Article Online
DOI: 10.1039/D6TA03387C

FTIR bands for Ni-imidazole coordination revealed important features. Weak bands corresponding to the C-H stretching vibrations of the aromatic imidazole ring appeared in the 3100–2900 cm^{-1} region. The band at 1590 cm^{-1} was assigned to the C=N stretching vibration of the imidazole ring. This band is red-shifted by ~30 40 cm^{-1} compared to free imidazole (~1625 cm^{-1}), consistent with coordination of the nitrogen atom to the Ni(II) center and in agreement with values reported for imidazolate-based MOFs in the literature. [47] This shift confirms the formation of metal–ligand coordination bonds within the BioMOF structure.

Additionally, the carboxylate groups in the protein contributed bands at 1547 cm^{-1} (asymmetric stretching) and 1455 cm^{-1} (symmetric stretching), highlighting their interaction with the nickel ion. Out-of-plane deformation vibrations of the imidazole ring were observed at 740 cm^{-1} and 662 cm^{-1}, while the formation of the Ni-N bond introduced a characteristic symmetric stretching band at 620 cm^{-1}, providing further evidence of successful coordination.[48]

Inductively coupled plasma–optical emission spectrometry (ICP-OES) analysis determined that the nickel loading in the Ni-ELF systems was 9% (w/w%) for **Ni-ELF 1** and **Ni-ELF 3**, whereas **Ni-ELF 2** exhibited a loading of 8% (w/w) (Table S1).

On the other hand, the volume and pore size of adsorbents play a crucial role in determining the adsorption properties of metal–organic frameworks (MOFs). To evaluate these properties, isothermal nitrogen (N_2) adsorption–desorption analysis was carried out on the Ni-ELF catalysts (Figure 3c, Figure S5). The Brunauer–Emmett–Teller (BET) surface area of **Ni-ELF 1** was the highest (139 m^2/g), providing a larger specific surface area and more accessible sites for adsorption–desorption interactions. **Ni-ELF 3** exhibited

View Article Online
DOI: 10.1039/D6TA03387C

an intermediate value (111 m²/g), while **Ni-ELF 2** showed almost half the area of **Ni-ELF 1** (82 m²/g), corresponding to the lowest surface availability.

In addition, the porosity and pore volume were determined using the Barrett–Joyner–Halenda (BJH) method, revealing an average pore diameter ranging from 3 to 6 nm and pore volumes between 0.17 and 0.22 cm³/g (Figure 3d, Table S2, Figures S6–S8). All samples displayed type IV adsorption–desorption isotherms, classifying them as mesoporous materials according to IUPAC standards.[49] These results confirm that the synthesized Ni-ELF catalysts possess a well-defined porous structure, making them suitable for a variety of applications.

View Article Online
DOI: 10.1039/D6TA03387C

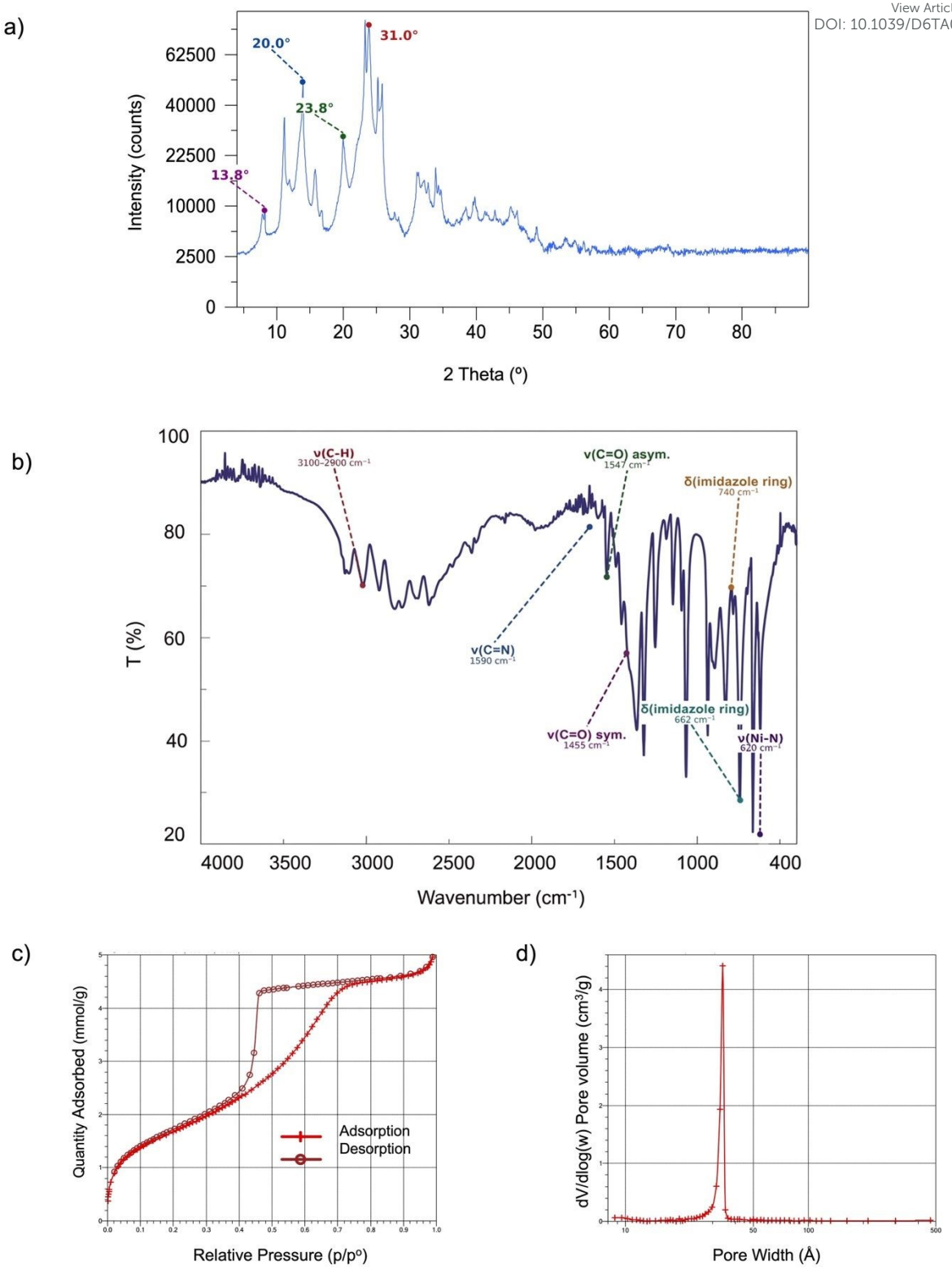

Figure 3. Characterization of **Ni-ELF 1**; a) XRD pattern; b) FT-IR spectrum; c) N_2 adsorption/desorption isotherm; d) BHJ desorption dV/dlog(W) pore volume (pore size).

View Article Online
DOI: 10.1039/D6TA03387C

Scanning electron microscopy (SEM) analysis of the Ni-ELFs revealed the formation of microsnowflake-like structures with six-fold symmetrical branches (Figures 4, S9). However, slight differences were observed depending on the enzyme employed. In the case of **Ni-ELF 1**, the microsnowflakes were approximately 13 μm in size, forming bilayers that were uniformly distributed across the surface, with some appearing clustered while others were more dispersed. For **Ni-ELF 2** and **Ni-ELF 3**, the microsnowflakes were smaller (≈9 μm) and tended to form multilayers (3–6 layers), resulting in a more aggregated arrangement (Figures S10–S11). This distinctive morphology provides a high surface area and mesoporosity, offering multiple edges and vertices that may serve as catalytically active sites.

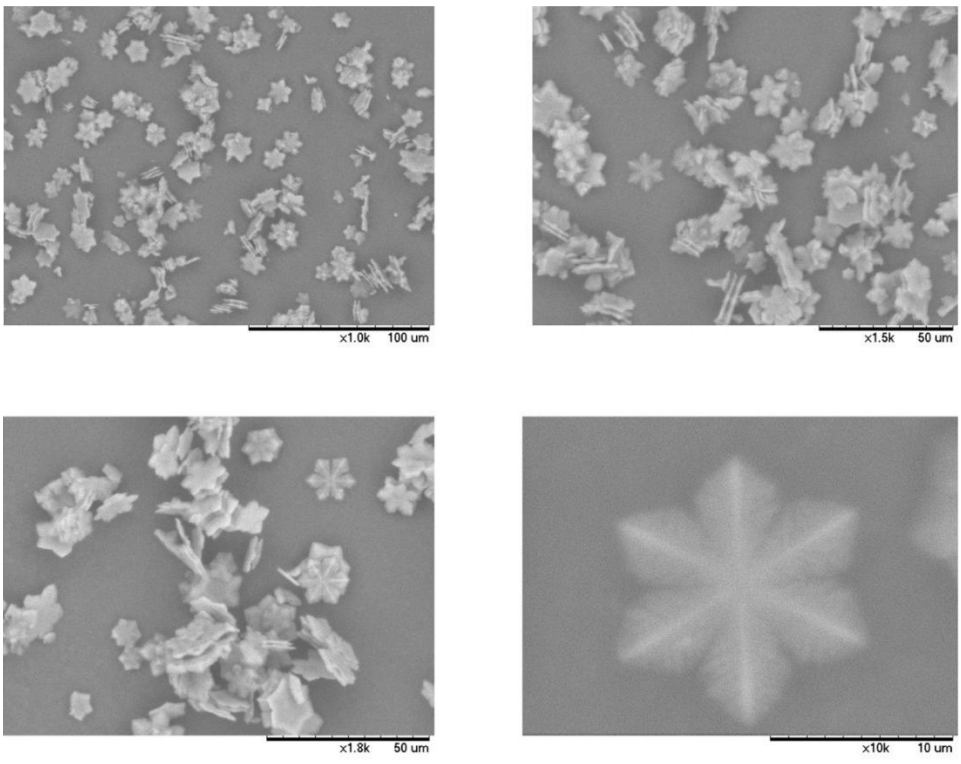

Figure 4. Scanning electron microscopy (SEM) images of **Ni-ELF 1** at different magnifications

View Article Online
DOI: 10.1039/D6TA03387C

Furthermore, these results demonstrate that the enzyme is a critical factor in the formation of the of Ni–MOF observed structures. Indeed, a control synthesis under identical conditions but without the enzyme yielded hexagonal, rounded microstructures with lower crystallinity (Figure S12). This clear contrast confirms the essential role of the enzyme in directing the growth of the distinctive snowflake-like architectures.

Finally, to confirm the incorporation of the protein into the designed system, confocal microscopy analysis was performed using **Ni-ELF-1** as a model. For this purpose, the protein was marked prior to synthesis. CALB was marked with Alexa Fluor 700 (AF) via a conjugation reaction carried out at room temperature for 3 h and monitored by UV–vis spectroscopy (Figure S13). Successful marking was confirmed by an increase in the 700 nm emission peak relative to the initial value, indicating effective fluorophore binding to the protein. Excess unbound fluorophore was removed by dialysis, and the marked protein exhibited a characteristic blue coloration. The synthesis of **Ni-ELF 1** was then carried out following the established protocol. Preservation of the **Ni-ELF-1** structure after AF incorporation in the protein was verified by FT-IR and SEM analyses, confirming that the ELF system was successfully obtained (Figure S14-S15). The resulting samples were examined by confocal microscopy to assess the presence and distribution of the protein within the system. Fluorescence imaging clearly confirmed that the enzyme was not only present but also incorporated into the framework, acting as an integral structural component. Morphologically, microflakes observed from the top view consisted of a single layer, whereas side views revealed two layers, as confirmed by Z-stack and orthogonal view analyses (Figure 5, Figures S16–S17). Distinct micro-snowflake morphologies were identified, some featuring central pores of varying shapes. Notable examples included hexagonal pores with spike-like projections and arrangements of

View Article Online
DOI: 10.1039/D6TA03387C

interconnected hexagons with pointed extensions. Each microsnowflake exhibited a unique and well-defined architecture.

When these structures were compared with those obtained in the enzyme-free system (Ni–MOF), a striking difference became evident: in the absence of the enzyme, the morphology appeared significantly more rounded and less crystalline, as confirmed by confocal analysis (Figures S18–S19). These observations provide strong evidence that the enzyme plays a crucial role in directing the formation and organization of the structures. To the best of our knowledge, this is the first report describing an enzyme as an integral structural component of an organic ligand framework.

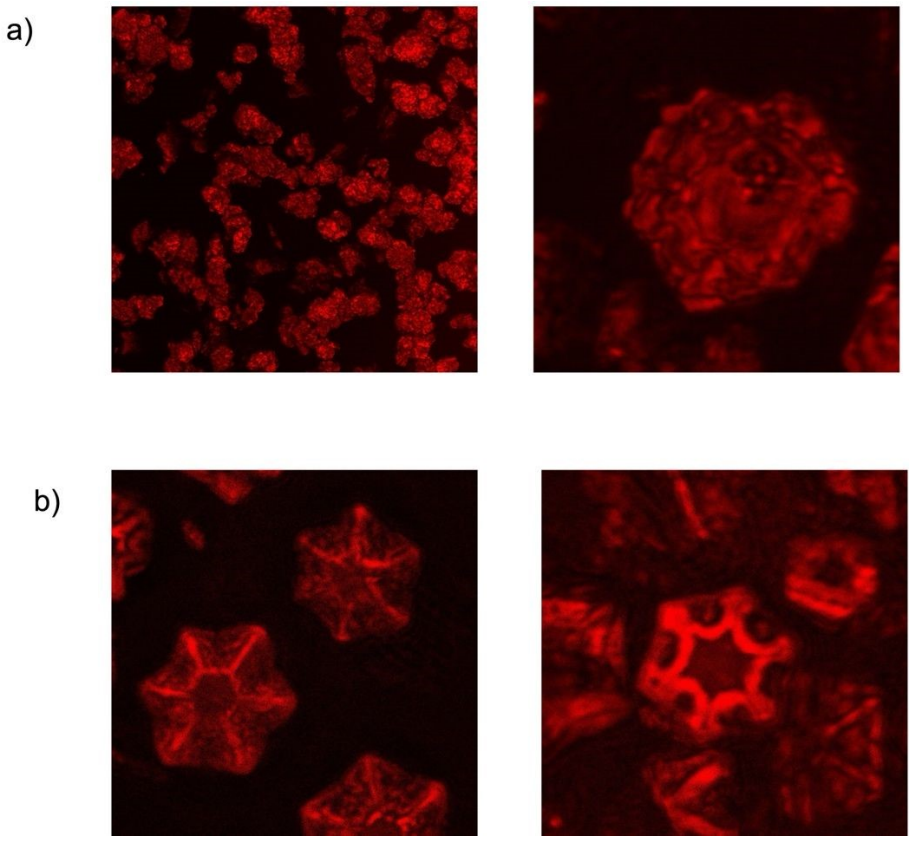

Figure 5. Confocal Z-stack images of the a) Enzyme-free system (Ni-MOF) and b) **Ni-ELF 1** hybrid. See experimental part for analytical conditions.

View Article Online
DOI: 10.1039/D6TA03387C

Thermal stability

Next, the thermal stability of the Ni-ELF materials was evaluated using **Ni-ELF 1** as a representative BioMOF to determine whether its formation contributed to enzyme stabilization. To this end, **Ni-ELF 1** was compared with the well-known free hydrolases, CALB and the thermoalkalophilic lipase GTL at 60 and 80 °C (Figure S20a), after 1 h of incubation. Residual activity was calculated relative to the initial activity at 25 °C, normalized to the specific activity toward p-nitrophenyl decanoate (*p*NPD) hydrolysis at this temperature, enabling assessment of the stabilizing effect imparted by the BioMOF architecture.

At 60 °C, **Ni-ELF 1** retained 66% of its initial activity, whereas free CALB retained only 9%, indicating a more than sevenfold increase in thermal stability upon BioMOF formation. At 80 °C, **Ni-ELF 1** still preserved 33% of its initial activity, outperforming both reference enzymes and exhibiting nearly fourfold higher residual activity than GTL, while free CALB was completely inactivated under these conditions.

To evaluate the structural stability of the material after thermal treatment, X-ray diffraction analyses were performed (Figure S20 b). The diffraction patterns recorded after incubation at 60 and 80 °C were virtually identical to that obtained at 25 °C, with no significant changes in peak position or intensity. These results indicate that the crystalline framework remained intact throughout the thermal stability experiments.

Adsorption of Aquatic Micropollutants on the BioMOF

The designed BioMOFs were evaluated as micromaterials for the adsorption of aquatic micropollutants. The adsorption performance of **Ni–ELF 1**, **Ni–ELF 2**, and **Ni–ELF 3**

View Article Online
DOI: 10.1039/D6TA03387C

was initially screened using Rhodamine B (RhB), a model pollutant frequently detected in aquatic environments at concentrations ranging from 0.014 to 0.14 ppm.[50] The different initial concentrations were selected based on solubility, optical response, and literature precedents for each pollutant, ensuring reliable kinetic monitoring without signal saturation in UV–vis measurements. The results revealed that pollutant removal is predominantly governed by adsorption rather than catalytic degradation.

Among the evaluated materials, **Ni–ELF 1** exhibited the highest performance, achieving 28% removal of RhB (50 ppm) within 20 min (42 ppm·h^{-1}); (Figures 6, S21), whereas **Ni–ELF 2** and **Ni–ELF 3** showed significantly lower efficiencies (14% and 12%, respectively). This enhanced behavior could be attributed to the lower degree of stacking and improved accessibility of adsorption sites in **Ni–ELF 1**. The addition of H_2O_2 (250 mM) resulted in only a slight increase in conversion (32% after 20 min; Figure S22), confirming adsorption as the dominant mechanism.

Based on these results, **Ni–ELF 1** was selected as the model material for further studies using a representative set of micropollutants, including phenol, *p*-aminophenol (pAP), and *p*-benzoquinone (*p*-BQ), chosen for their differences in molecular size, polarity, and environmental relevance.[51-53]

The adsorption kinetics were analyzed using the pseudo-second order (PSO) model, showing good linearity when plotting t/q□ *versus* t, consistent with a chemisorption-controlled process (Figures S23–S26). The corresponding equilibrium adsorption capacities (q_e) and rate constants (k_2) are summarized in Table 1.

View Article Online
DOI: 10.1039/D6TA03387C

Table 1. Equilibrium adsorption (q_e) and pseudo-second-order rate constants (k_2) for the compounds.

Compound	q_e (mg·g^{-1})	k_2(g·mg^{-1}·min^{-1})	Interpretation
*p*AP	20	0.02	Ultrarapid adsorption
Phenol	19.5	0.015	High affinity
p-BQ	17	0.008	Moderate
RhB	0.65	0.002	Limited

As shown in Figure 6, phenol—an environmentally relevant pollutant with acute toxicity around 5 ppm and typical concentrations between 0.1 and 1 ppm[54]—was rapidly adsorbed, reaching 47% removal within 1 min (47 ppm·min^{-1}) and complete removal after 20 min (Figure S27). The PSO model yielded a high-rate constant (k_2 = 0.015 g·mg^{-1}·min^{-1}), indicating strong interactions with the BioMOF surface.

Similarly, *p*-aminophenol (*p*AP), commonly detected at concentrations around 0.5 ppm in water systems[55], achieved 44% removal within 1 min (44 ppm· min^{-1}) and complete removal after 20 min (Figure S28), with the highest rate constant (k_2 = 0.02 g·mg^{-1}·min^{-1}), consistent with ultrarapid adsorption.

In contrast, *p*-benzoquinone (*p*-BQ), a highly toxic oxidation intermediate[56], exhibited moderately slower kinetics, reaching 35% removal within 1 min and 82% after 20 min (Figure S29), with a lower rate constant (k_2 = 0.008 g·mg^{-1}·min^{-1}), suggesting weaker affinity.

Rhodamine B, the largest molecule tested (≈1.5 × 1.0 × 0.7 nm), showed the slowest adsorption and partial reversibility over time (50 ppm, Figure S30). The PSO model

View Article Online
DOI: 10.1039/D6TA03387C

yielded the lowest rate constant (k_2 = 0.002 g·mg^{-1}·min^{-1}), indicating that adsorption is mainly limited by weaker host–guest interactions rather than diffusion constraints, despite the relatively large pore size (~3 nm) of **Ni–ELF 1**.

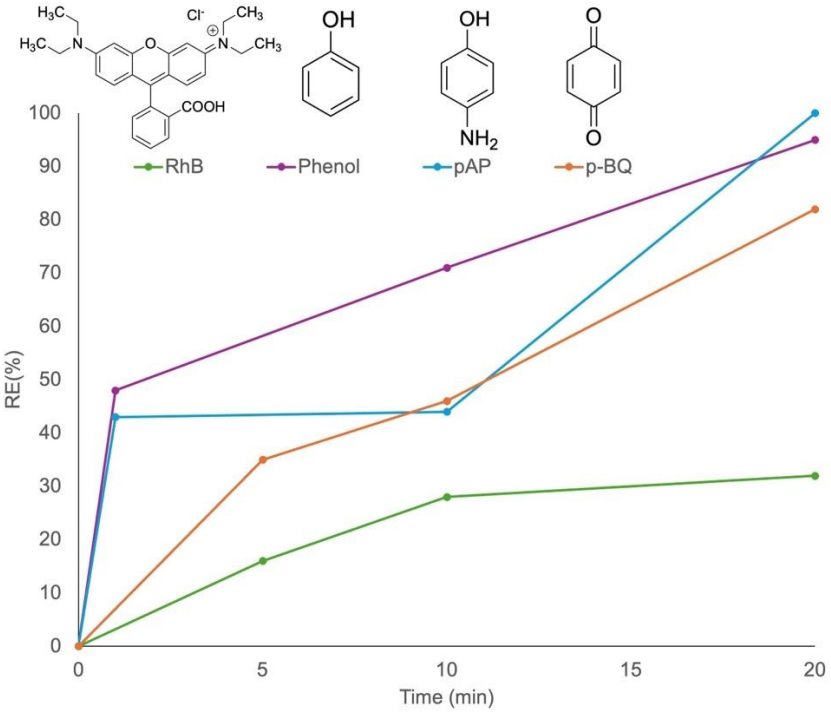

Figure 6. Adsorption of different micropollutants using **Ni-ELF 1**, expressed as removal efficiency (%), from aqueous solutions of RhB (50 ppm), phenol (100 ppm), *p*-aminophenol (100 ppm), and *p*-benzoquinone (100 ppm).

The observed differences in adsorption kinetics are governed by the interplay of multiple interactions between pollutants and the BioMOF surface. Likely mechanisms include coordination with Ni^{2+} centers (particularly for phenol, *p*AP, and p-BQ), π–π stacking with imidazole ligands, hydrogen bonding with CALB residues (Ser, Thr, Asp, Glu, Tyr), and electrostatic interactions in the case of cationic RhB.[57-58] Washing experiments confirmed the robustness of these interactions, as negligible desorption was observed upon treatment with water, 1% (v/v) Tween 20, ethanol, acetonitrile, or 100 mM NaCl

View Article Online
DOI: 10.1039/D6TA03387C

(data not shown). Phenol was the only compound showing partial desorption, reaching approximately 50% upon washing with pure acetonitrile, suggesting comparatively weaker interactions. In contrast, all other compounds remained firmly bound, exhibiting negligible desorption under all tested conditions (data not shown).

To evaluate the reusability of the material, a recycling experiment was conducted for phenol. After adsorption, the MOF was recovered, washed with acetonitrile, and reused in a second cycle. Importantly, the catalyst retained 100% of its initial adsorption activity after this regeneration step, confirming its full recyclability under these conditions (Figure S31). Only one recycling cycle was performed, since additional washing cycles with the organic solvent led to structural instability of the material, likely due to partial degradation under prolonged exposure. Nevertheless, these results demonstrate that a single mild regeneration step is sufficient to fully restore performance without loss of activity.

Overall, these results demonstrate the versatility and especially the efficiency of Ni–ELF 1 in water remediation, achieving in some cases, within one minute the removal of key micropollutants at concentrations over 50-100 times higher than the maximum permitted limits.

Application of ELF for the Removal of other Contaminants: pET-ase–Like Activity

The catalytic performance of the **Ni–ELF** materials was systematically evaluated by assessing their hydrolase-like activity using *p*-nitrophenyl decanoate (*p*NPD, C10) as a model substrate. Among the three synthesized materials, only **Ni–ELF 1** exhibited measurable catalytic activity, with a specific activity of 2.92 $U \cdot mg^{-1}$, whereas **Ni–ELF 2** and **Ni–ELF 3** showed no detectable conversion. This marked difference highlights the

View Article Online
DOI: 10.1039/D6TA03387C

critical role of structural features, such as higher specific surface area and reduced aggregation, in enhancing the accessibility of active sites. Consequently, **Ni–ELF 1** was selected as the most suitable candidate for further catalytic applications.

As a proof of concept, the catalytic potential of Ni–ELF 1 was further explored in the depolymerization of PET using real plastic bottle fragments under mild aqueous conditions. The degradation process was monitored by SEM, UV–Vis, and FT-IR analyses of both the solid residues and the liquid phase.[59–60] The combined data revealed progressive polymer depolymerization, evidenced by the fragmentation of PET into smaller particles (approximately 50 μm), observed in the aqueous soluble fraction by UV and SEM analyses, and by FT-IR of the solid (Figures S32–S35). FT-IR showed the decrease in C=O, C-O signal in the treated PET, demonstrating the reduction in ester bonds on the polymer because of the hydrolysis catalyzed by Ni catalyst. SEM images showed the formation of microplastic particles on the solution and the presence of terephthalic acid by UV. The catalytic performance was found to be highly dependent on the reaction conditions, as summarized in Table S3. Initial experiments using large PET fragments under ambient conditions resulted in limited degradation (~1% w/w after 28 days), although clear evidence of polymer transformation was observed (Figure S33).

Subsequent optimization studies investigated the effect of different additives on PET degradation efficiency. First, Triton X-100 was evaluated, as previous esterase and lipase activity assays had shown that this non-ionic surfactant enhances the activity of the immobilized enzymes. Its addition significantly improved the degradation performance [61] (Figure S34–S38). This effect is likely related to improved substrate accessibility and stabilization of the enzyme in a more active conformation.

View Article Online
DOI: 10.1039/D6TA03387C

Subsequently, NaOH was tested as an additive, since most reported PET degradation systems rely on alkaline conditions to promote base-catalyzed ester hydrolysis. Accordingly, reactions were performed in the presence of 0.1 M NaOH to benchmark the enzymatic system against this chemical approach.[62-63] However, no improvement in catalytic efficiency was observed under alkaline conditions, suggesting that the reaction proceeds independently of base-catalyzed hydrolysis under the conditions tested.

In addition, variations in buffer conditions (phosphate buffer, pH 7) did not lead to any noticeable enhancement in catalytic performance. These results indicate that neither alkaline nor buffer modifications improve the intrinsic catalytic efficiency of the system. In contrast, reducing the size of PET fragments and increasing catalyst loading had a positive effect on degradation, highlighting the importance of surface accessibility.

Under optimized conditions (small PET fragments, 300 mg of catalyst, 0.025% (v/v) Triton X-100, and 60 °C), up to 8% (w/w) PET degradation was achieved after 93 h, corresponding to 5.4 μmol of degraded PET and a productivity of 135 nmol of degradation products mL^{-1} day^{-1} (Figure S39–S40).

Although the overall degradation efficiency remains moderate, these results demonstrate that **Ni–ELF 1** behaves as a hybrid catalyst with PETase-like activity under mild and sustainable conditions. The reaction proceeds in a dispersed heterogeneous system, where the polymer is introduced as an emulsion-like phase, enhancing interfacial contact and enabling effective catalytic interaction between the solid components.

Unlike many reported methods that rely on pretreated PET (films, powders, or fibers) and often require harsh reaction conditions (Table 2), our approach enables the direct degradation of real plastic fragments in aqueous media without any preprocessing steps

View Article Online
DOI: 10.1039/D6TA03387C

(Table 2). This represents a clear advantage in terms of operational simplicity, sustainability, and practical applicability.

Moreover, these findings highlight the distinctly multifunctional nature of Ni–ELF materials. Beyond their established role as highly efficient adsorbents for micropollutant removal, they also demonstrate strong performance in plastic degradation. Altogether, this positions our system as a more versatile and promising alternative to conventional strategies, with significant potential for integrated environmental remediation applications.

Table 2. PET degradation under different conditions of reported methods in the literature.[64-67]

PET sample	Catalyst	Additive	Temperature (ºC)	Pressure /Light	Time	PET degradation (%)	Reference
Granular PET	$ZnCl_2/H_2O$	Water	160	n.a	8 h	0.03	64
PET from plastic bottle	Lipase from *Aspergillus Niger*	NaOH 1M	37	n.a	28 days	3.80	65
PET pellets	$SiW_{11}Ni$	Water	190	n.a	30 min	1.63	66
PET microfiber	$Ni_5P_4/TiO_2/CNFs$	5 M KOH	25	500 W mercury light	12 h	6.23	67
PET from plastic bottle	ELF-1	0.025% (v/v) Triton X-100	25	-	93h	8	Our work

Conclusions

View Article Online
DOI: 10.1039/D6TA03387C

In this work, we report for the first time the design and synthesis of a novel Ni MOFs-type materials using enzymes as ligand, denoted as **Ni–ELF** (Nickel Enzyme–Ligand Framework), in which the enzyme serves as an integral structural component. **Ni–ELF** materials exhibit distinctive micro-snowflake-like morphologies with six-fold symmetrical branches, whose size and layering depend directly on the enzyme identity. **Ni–ELF 1** formed larger bilayer flakes (~13 μm), whereas **Ni–ELF 2** and **Ni–ELF 3** yielded smaller (~9 μm) multilayer structures, confirming that the enzyme dictates the architecture of the resulting BioMOFs. These materials are mesoporous, with **Ni–ELF 1** displaying the highest specific surface area, and confocal microscopy confirmed the enzyme's structural integration.

Ni–ELF materials, particularly **Ni–ELF 1**, demonstrated excellent performance as materials for the removal of aquatic micropollutants, with adsorption predominantly governed by chemisorption. Notably, **Ni–ELF 1** achieved complete removal of phenol and *p*-aminophenol within 20 minutes, with rapid initial uptake (≈47% and 44% removal within 1 minute, respectively) and high pseudo-second-order rate constants (k_2 = 0.015–0.02 $g \cdot mg^{-1} \cdot min^{-1}$), highlighting its high affinity toward these contaminants. In contrast, bulkier molecules such as Rhodamine B exhibited lower adsorption capacity (q_e = 0.65 $mg \cdot g^{-1}$), underscoring the influence of molecular size on adsorption efficiency.

As a proof of concept, the potential of **Ni–ELF 1** for the direct depolymerization of plastic bottle pieces was also demonstrated, producing 5.4 μmoles of degraded PET with a productivity of 135 nmoles of degradation products $\cdot mL^{-1} \cdot day^{-1}$.

These results further demonstrate the high potential of **Ni–ELF 1** as an efficient hybrid biocatalyst exhibiting PETase-like activity, while also functioning as a versatile adsorbent for environmental remediation. The eco-friendly, simple, and sustainable synthesis

View Article Online
DOI: 10.1039/D6TA03387C

protocol, demonstrated by the preparation of gram quantities on a small scale with high reproducibility, makes this a strong candidate for the scalable production of MOFs for future industrial applications.

These findings establish **Ni–ELF** systems as a novel class of enzyme–metal frameworks in which the enzyme acts as a structural guide, governing material formation, morphology, and catalytic and adsorption behavior. In contrast to conventional enzyme–MOF systems based on preformed supports such as NH-MIL-53(Al), Fe-BTC, ZIF-8, or Cu-BTC—where the enzyme is typically immobilized to preserve activity—Ni–ELFs arise from a cooperative assembly process in which the biomolecule actively directs the framework architecture. Notably, while enzyme–MOF composites have been widely reported, nickel-based systems remain extremely scarce, underscoring the distinctive nature of this approach.

Moreover, their tunable architecture and intrinsic porosity open promising avenues beyond aqueous-phase applications, particularly in gas capture and storage (e.g., CO_2 adsorption), as well as in molecular separation and sensing technologies. By tailoring both the enzyme component and the metal framework, Ni–ELF BioMOFs could evolve into multifunctional platforms that integrate catalytic performance with structural adaptability, with broad implications for sustainable catalysis, environmental remediation, and advanced materials engineering.

Author contributions

J.M.P. conceived the project. J.M.P. supervised the project and obtained funding. C.G-S performed material synthesis, characterization, and catalytic reactions. J.M.P and C.G-S. analysed the data and wrote the manuscript.

View Article Online
DOI: 10.1039/D6TA03387C

Conflicts of interest

There are no conflicts to declare'.

Data availability

The data that support the findings of this study are available in the supplementary information (SI) of this article. Supplementary information: Additional data of synthetic procedure of the Ni-ELF MOFs, characterization (XDR, BET, SEM, Confocal fluorescence), thermal stability assays and additional data of adsorption of aquatic micropollutans and procedure of PET degradation.

Acknowledgments

The authors thank the support of the Spanish National Research Council (CSIC) and the Ministry of Science (projects Intramural Grant, 202480e088). The authors thank Dr. Martinez from Novonesis for the gift of the enzymes. Additionally, the authors appreciate the support for the publication fee provided by the CSIC Open Access Publication Support Initiative through its Unit of Information Resources for Research (URICI).

Nomenclature

AF – Alexa Fluor 700

AF–CALB – Alexa Fluor 700–Candida antarctica Lipase B conjugate

BET – Brunauer–Emmett–Teller (surface area analysis method)

BioMOF – Biological Metal–Organic Framework

BJH – Barrett–Joyner–Halenda (pore size distribution method)

View Article Online
DOI: 10.1039/D6TA03387C

CALB – Candida antarctica Lipase B (Lipozyme® CalB)

CAT – Catalase (Catazyme 25 L)

CNFs – Carbon Nanofibers

CO_2 – Carbon dioxide

Cu-BTC – Copper benzene-1,3,5-tricarboxylate MOF

DMSO – Dimethyl sulfoxide

ELF – Enzyme–Ligand Framework

Fe-BTC – Iron benzene-1,3,5-tricarboxylate MOF

FLIM – Fluorescence Lifetime Imaging Microscopy

FT-IR – Fourier Transform Infrared Spectroscopy

GOx – Glucose oxidase (Gluzyme® Mono 10000 BG)

H_2O_2 – Hydrogen peroxide

HCl – Hydrochloric acid

HPLC – High-Performance Liquid Chromatography

ICP-OES – Inductively Coupled Plasma–Optical Emission Spectroscopy

IUPAC – International Union of Pure and Applied Chemistry

k_2 – Pseudo-second-order rate constant

MOF – Metal–Organic Framework

M_{PET} – Molecular weight of PET (192 g/mol)

N_2 – Nitrogen gas

NaCl – Sodium chloride

NaOH – Sodium hydroxide

NH-MIL-53(Al) – Amino-functionalized aluminum MIL-53 MOF

Ni-ELF – Nickel Enzyme–Ligand Framework

$NiCl_2 \cdot 6H_2O$ – Nickel(II) chloride hexahydrate

View Article Online
DOI: 10.1039/D6TA03387C

Ni-MOF – Nickel-based Metal–Organic Framework

***p*AP** – para-Aminophenol

PET – Polyethylene terephthalate

PETase – PET-degrading enzyme

***p*NPD** – para-Nitrophenyl decanoate

***p*-BQ** – para-Benzoquinone

PSO – Pseudo-second-order (kinetic model)

q_e – Equilibrium adsorption capacity (mg pollutant/g BioMOF)

q_t – Amount of contaminant adsorbed at time t ($mg \cdot g^{-1}$)

RE – Removal Efficiency (%)

RhB – Rhodamine B

SDS-PAGE – Sodium Dodecyl Sulfate–Polyacrylamide Gel Electrophoresis

SEM – Scanning Electron Microscopy

SI – Supplementary Information

URICI – Unit of Information Resources for Research

UV–Vis – Ultraviolet–Visible spectroscopy

XRD – X-ray Diffraction

ZIF-8 – Zeolitic Imidazolate Framework-8

References

[1] H. Furukawa, K. E. Cordova, M. O'Keeffe, O. M. Yaghi, *Science*, 2013, **341**, 1230444.
[2] O. Yaghi, M. O'Keeffe, N. W. Ockwig *et al.*, *Nature*, 2003, **423**, 705–714.
[3] D. Li, A. Yadav, H. Zhou, K. Roy, P. Thanasekaran, C. Lee, *Clean. Mater.*, 2024, **8**, 2300244.
[4] V. F. Yusuf, N. I. Malek, S. K. Kailasa, *ACS Omega*, 2022, **7**, 44507–44531.
[5] N. L. Rosi, J. Eckert, M. Eddaoudi, D. T. Vodak, J. Kim, M. O'Keeffe, O. M. Yaghi, *Science*, 2003, **300**, 1127–1129.
[6] N. Singh, S. Qutub, N. M. Khashab, *J. Mater. Chem. B*, 2021, **9**, 5925–5934.
[7] J. Y. Oh, Y. Sim, G. Yang, M.-H. Park, K. Kim, J.-H. Ryu, *Inorg. Chem. Front.*, 2024, **11**, 3119–3135.
[8] P. Pachfule, T. Panda, C. Dey, R. Banerjee, *CrystEngComm*, 2010, **12**, 2381–2389.

View Article Online
DOI: 10.1039/D6TA03387C

[9] M. Burigan, H. Wang, J. Elmroth Nordlander, O. M. Yaghi, *Inorg. Chem.*, 2025, **64**, 5561–5567.
[10] A. Ali, M. Muslim, I. Neogi, M. Afzal, A. Alarifi, M. Ahmad, *ACS Omega*, 2022, **7**, 24438–24451.
[11] J. Liu, G. Xing, L. Chen, *Acc. Chem. Res.*, 2024, **57**, 1032–1045.
[12] K. Suresh, C. A. Carey, A. J. Matzger, *Cryst. Growth Des.*, 2024, **24**, 2288–2300.
[13] H. Cai, Y.-L. Huang, D. Li, *Coord. Chem. Rev.*, 2019, **378**, 207–221.
[14] S. Rojas, T. Devic, P. Horcajada, *J. Mater. Chem. B*, 2017, **5**, 2560–2573.
[15] C. B. Jha, C. Singh, K. Manna, R. Mathur, *Med. Hypotheses*, 2024, **183**, 111252.
[16] S. Wu, Z. Sun, Y. Peng, Y. Han, J. Li, S. Zhu, Y. Yin, G. Li, *Biosens. Bioelectron.*, 2020, **169**, 112613.
[17] Y. Liu, S. Cui, W. Ma, Y. Wu, R. Xin, Y. Bai, Z. Chen, J. Xu, J. Ge, *J. Am. Chem. Soc.*, 2024, **146**, 12565–12576.
[18] S. Chand, O. Alahmed, W. S. Baslyman, A. Dey, S. Qutub, R. Saha, Y. Hijikata, M. Alaamery, N. M. Khashab, *J. Am. Chem. Soc.*, 2023, **145**, 7323–7330.
[19] S. Elmehrath, H. L. Nguyen, S. M. Karam, A. Amin, Y. E. Greish, *Nanomaterials*, 2023, **13**, 953.
[20] A. C. McKinlay, R. E. Morris, P. Horcajada, G. Férey, R. Gref, P. Couvreur, C. Serre, *Angew. Chem. Int. Ed.*, 2010, **49**, 6260–6266.
[21] B. M. Thamer, M. M. Abdul Hameed, *J. Inorg. Organomet. Polym.*, 2025, **35**.
[22] J. Navarro-Alapont, C. Negro, S. Navalón, A. Dhakshinamoorthy, D. Armentano, J. Ferrando-Soria, E. Pardo, *Inorg. Chem.*, 2024, **63**, 13681–13688.
[23] A. Mukhrjee, R. Dewangan, S. Naz, in *Metal Organic Frameworks: Fundamentals to Advanced*, 2024, pp. 25–42.
[24] X. Wang, P. C. Lan, S. Ma, *ACS Cent. Sci.*, 2020, **6**, 1497–1506.
[25] R. Murty, M. K. Bera, I. M. Walton, C. Whetzel, M. R. Prausnitz, K. S. Walton, *J. Am. Chem. Soc.*, 2023, **145**, 7323–7330.
[26] W. Xu, Y. Wu, L. Jiao *et al.*, *Nano Res.*, 2023, **16**, 3364–3371.
[27] J. M. Palomo, *Chem. Commun.*, 2019, **55**, 9583–9589.
[28] C. Garcia-Sanz, J. M. Palomo, *ACS Sustainable Chem. Eng.*, 2024, **12**, 13678–13686.
[29] A. Helal, S. S. Shah, M. Usman, M. Y. Khan, M. A. Aziz, M. Rahman, *Chem. Rec.*, 2022, **22**, e202200055.
[30] Q. Yin, Z. Song, S. Yang, G.-D. Wang, Y. Sui, J. Qi, D. Zhao, L. Hou, Y.-Z. Li, *Chem. Sci.*, 2023, **14**, 5643–5649.
[31] M. Yan, Y. Yang, F. Chen, D. Hantoko, A. Pariaramby, E. Kanchanatip, *Environ. Sci. Pollut. Res.*, 2023, **30**, 102560–102573.
[32] J. Aguila-Rosas, F. J. Cano, A. Nagaya, C. T. Quirino-Barreda, M. J. Martínez Ortiz, A. Guzmán Vargas, I. A. Ibarra, E. Lima, *Chem. Commun.*, 2025, **61**, 11706–11731.
[33] Y. Gao, L. Zheng, L. Duan, J. Bi, *Langmuir*, 2024, **40**, 15365–15388.
[34] A. Kharkova, V. Arlyapov, A. Medvedeva, R. Lepikash, P. Melnikov, A. Reshetilov, *Sensors*, 2022, **22**, 8522.
[35] M. Patel, R. Kumar, K. Kishor, T. Mlsna, C. U. Pittman Jr., D. Mohan, *Chem. Rev.*, 2019, **119**, 3510–3673.
[36] Q. Hu, L. Hao, *Water*, 2025, **17**, 2335.
[37] S. Satyam, S. Patra, *Heliyon*, 2024, **10**, e29573.
[38] A. O. C. Iroegbu, M. L. Teffo, E. R. Sadiku *et al.*, *npj Clean Water*, 2025, **8**, 85.
[39] C. Yan, J. Jin, J. Wang, F. Zhang, Y. Tian, C. Liu, F. Zhang, L. Cao, Y. Zhou, Q. Han, *Coord. Chem. Rev.*, 2022, **468**, 214595.

[40] S. Ramanayaka, M. Vithanage, A. Sarmah, T. An, K.-H. Kim, Y. S. Ok, *RSC Adv.*, 2019, **9**, 34359–34376.
[41] A. A. Mohammadi, Z. Niazi, K. Heidari, A. Afarinandeh, M. Samadi Kazemi, G. A. Haghighat, Y. Vasseghian, S. Rezania, A. Barghi, *Environ. Res.*, 2022, **212**, 113164.
[42] I. Ramírez, J. Padilla, A. L. Villa, *Catalysts*, 2026, **16**, 240.
[43] G. Karthikeyan, S. Mohan, R. G. Balakrishna, *ACS Appl. Nano Mater.*, 2025, **8**, 12966–12979.
[44] I. D. Vlaicu, R. Olar, G. V. Scaeteanu, L. Silvestro, M. Maurer, N. Stanica, M. Badea, *J. Therm. Anal. Calorim.*, 2018, **134**, 503–512.
[45] S. Zhang, S. Wang, Y. Wen, K. Jiao, *Molecules*, 2003, **8**, 866–872.
[46] Z. Liu, G. Li, M. R. Alalouni, Z. Chen, X. Dong, J. Wang, C. Chen, *Chem. Commun.*, 2024, **60**, 188.
[47] F. Kümbetlioğlu, K. O. Oskay, Z. Çıplak, A. Ateş, *ACS Omega*, 2023, **8**, 27650–27662.
[48] M. Zeraati, V. Alizadeh, P. Kazemzadeh, M. Safinejad, H. Kazemian, G. Sargazi, *J. Porous Mater.*, 2022, **29**, 257–267.
[49] L. Xu, J. Zhang, J. Ding, T. Liu, G. Shi, X. Li, W. Dang, Y. Cheng, R. Guo, *Minerals*, 2020, **10**, 72.
[50] M. M. Hossain, S. Asghar, D. Mohotti, T. Robi, S. Wu, *Results Eng.*, 2025, **26**, 104790.
[51] A. Goel, M. Rani, *Environ. Qual. Manage.*, 2024, **34**, e22205.
[52] D. Xu, H. Ma, *J. Clean. Prod.*, 2021, **313**, 127758.
[53] R. L. Ramos, V. R. Moreira, M. C. S. Amaral, *J. Environ. Manage.*, 2024, **351**, 119772.
[53] D. Yu, J. Li, Z. Kang, L. Liu, J. He, Y. Fang, H. Yu, S. Dong, *Analyst*, 2020, **145**, 5266–5272.
[54] M. Rapiya, M. Slayi, W. Truter, *Discov. Water*, 2025, **5**, 69.
[55] C. F. Yin, P. Pan, T. Li, X. Song, Y. Xu, N. Y. Zhou, *Microbiome*, 2025, **13**, 1.
[56] N. R. Nicomel, L. Y. Li, B. A. Mohamed, S. S. Ramim, *J. Environ. Manage.*, 2022, **316**, 115263.
[57] R. Bruno, T. F. Mastropietro, G. De Munno, D. Armentano, *Molecules*, 2021, **26**, 4594.
[58] E. Kopcsik, Z. Mucsi, R. Schiwert *et al.*, *Sci. Rep.*, 2025, **15**, 629.
[59] G. Karthikeyan, S. Mohan, R. G. Balakrishna, *Spectrochim. Acta A*, 2015, **139**, 229–242.
[60] S. G. Prasad, A. De, U. De, *Int. J. Spectrosc.*, 2011, **2011**, 810936.
[61] J. M. Palomo, M. Filice, O. Romero, J. M. Guisan, *Methods Mol. Biol.*, 2013, **1051**, 255–273.
[62] Y. Wang, Y. Zhang, H. Song, Y. Wang, T. Deng, X. Hou, *J. Clean. Prod.*, 2019, **208**, 1469–1475.
[63] M. E. Sevilla, M. D. Garcia, Y. Perez-Castillo, V. Armijos-Jaramillo, S. Casado, K. Vizuete, A. Debut, L. Cerda-Mejía, *Polymers*, 2023, **15**, 1779.
[64] A. Safdar, F. Ismail, M. Imran, *Environ. Adv.*, 2024, **17**, 100563.
[65] P. Fang, B. Liu, J. Xu, Q. Zhou, S. Zhang, J. Ma, X. Lu, *Polym. Degrad. Stab.*, 2018, **156**, 22–31.
[66] G. Peng, X. Qi, W. Qu, X. Shao, L. Song, P. Du, J. Xiong, *Catal. Sci. Technol.*, 2023, **13**, 5868–5879.
[67] Q. Chen, H. Yan, K. Zhao, S. Wang, D. Zhang, Y. Li, R. Fan, J. Li, X. Chen, X. Zhou, Y. Liu, X. Feng, D. Chen, C. Yang, *Nat. Commun.*, 2024, **15**, 10732.

View Article Online
DOI: 10.1039/D6TA03387C

View Article Online
DOI: 10.1039/D6TA03387C

Data Availability Statement

The data supporting this article have been included as part of the Supplementary Information.